applied optics

X-ray phase imaging with the unified modulated pattern analysis of near-field speckles at a laboratory source

M.-C. Zdora,[1,*] I. Zanette,[1] T. Walker,[1] N. W. Phillips,[2] R. Smith,[1] H. Deyhle,[1,3] S. Ahmed,[1,3] and P. Thibault[1,3]

[1]Physics and Astronomy, University of Southampton, Highfield Campus, Southampton SO17 1BJ, UK
[2]Department of Engineering Science, University of Oxford, Parks Road, Oxford OX1 3PJ, UK
[3]Diamond Light Source, Harwell Science and Innovation Campus, Fermi Ave., Didcot OX11 0DE, UK
*Corresponding author: m.zdora@soton.ac.uk

Received 27 November 2019; revised 29 January 2020; accepted 30 January 2020; posted 30 January 2020 (Doc. ID 384531); published 2 March 2020

X-ray phase-contrast techniques are powerful methods for discerning features with similar densities, which are normally indistinguishable with conventional absorption contrast. While these techniques are well-established tools at large-scale synchrotron facilities, efforts have increasingly focused on implementations at laboratory sources for widespread use. X-ray speckle-based imaging is one of the phase-contrast techniques with high potential for translation to conventional x-ray systems. It yields phase-contrast, transmission, and dark-field images with high sensitivity using a relatively simple and cost-effective setup tolerant to divergent and polychromatic beams. Recently, we have introduced the unified modulated pattern analysis (UMPA) [Phys. Rev. Lett. 118, 203903 (2017)], which further simplifies the translation of x-ray speckle-based imaging to low-brilliance sources. Here, we present the proof-of-principle implementation of UMPA speckle-based imaging at a microfocus liquid-metal-jet x-ray laboratory source.

https://doi.org/10.1364/AO.384531

1. INTRODUCTION

The conventional method of taking x-ray images based on absorption contrast has some inherent limitations leading to poor contrast from details with similar densities. A way to circumvent this problem is to increase the density of certain sample features with the use of contrast agents [1–3], but this procedure is not always possible, is often cumbersome and challenging, and generally alters the native structure of the specimen. It is, furthermore, incompatible with many follow-up and complementary analysis procedures.

It was first demonstrated over twenty years ago that, provided a certain level of coherence of the illuminating x-ray beam, images of superior quality can be obtained by exploiting the information from the phase shift of the x-rays as they travel through the investigated specimen, rather than solely the absorption signal [4,5]. A large number of full-field x-ray phase-contrast methods with high density sensitivity have been developed, mostly using the highly brilliant x-ray beams provided by synchrotron sources [6–11].

Nowadays, many synchrotron beamlines dedicated to imaging worldwide use established x-ray phase-contrast methods to generate two- and three-dimensional data for the visualization of the internal structure of specimens at different length scales, with applications in a broad range of disciplines, including materials science, biomedical imaging, paleontology, and geology (see, e.g., Refs. [12–17]). However, synchrotron sources are large-scale facilities with competitive access, and the use of x-ray phase-contrast imaging is still limited to a restricted user community.

Among the x-ray phase-contrast imaging methods tolerant to the polychromatic and divergent beams of laboratory sources [4,9,18], x-ray speckle-based imaging (SBI) has strong potential for translation to laboratory systems [19,20]. SBI overcomes some of the limitations of x-ray grating interferometry [18] or other grating-based methods [9], as well as propagation-based imaging [4]. While the first require expensive and absorbing optical elements that in general also limit the flexibility in the experimental geometry, the latter relies on high-resolution detectors and is sensitive only to the Laplacian of the phase shift induced by the sample.

SBI provides high-quality signals without the use of sophisticated optical elements or very precise instrumentation, and can be adapted to image large samples of up to a few centimeters in size. In its original implementation, SBI relies on the use of a

near-field speckle pattern [21] generated by a phase modulator or diffuser consisting of disordered, negligibly absorbing features, e.g., a piece of sandpaper, when illuminated by (partially) coherent x-rays. The transmission, differential phase, and small-angle scattering information (also called dark-field signal) of the sample are encoded in the speckle pattern and subsequently decoded using an appropriate algorithm [22].

Originally, two experimental implementations of SBI were proposed, single-shot "speckle tracking" [11,23] and multi-frame "speckle scanning," for which frames are recorded at different lateral positions of the phase modulator [10]. While in speckle-tracking SBI, the multimodal images are extracted from a single frame, but with limited spatial resolution [19], speckle-scanning methods provide higher spatial resolution data at the expense of a longer acquisition time and increased complexity of the setup [24]. The large number of frames required for speckle scanning is the main bottleneck for the implementation of high-resolution SBI at low-brilliance laboratory sources, where scans of several hours or days are required for a single projection.

The recently developed unified modulated pattern analysis (UMPA) for SBI is the ideal candidate for effective implementation of SBI at laboratory sources, as it merges the advantages of speckle-tracking and speckle-scanning SBI while mitigating their limitations [25]. Up until now, UMPA was implemented at synchrotron sources, where it has been employed for metrology purposes [26] and for virtual histology of *ex-vivo* animal tissues [27].

Here we present a proof-of-principle experiment that highlights the potential of the UMPA method for high-resolution SBI at a liquid-metal-jet microfocus x-ray laboratory source.

2. EXPERIMENTAL ARRANGEMENT AND DATA ACQUISITION

The measurements were performed with a liquid-metal-jet x-ray source by Excillum (Sweden, MetalJet D2) with ExAlloy I1 anode material composed of 68% (by weight) gallium, 22% (by weight) indium, and 10% (by weight) tin [28]. The source was operated at an accelerating voltage of 50 kV and with a current of 0.200 mA, giving a power of 10 W, with an average x-ray energy of approximately 20 keV. The nominal electron beam spot size was 5.7 μm × 5.7 μm.

The experimental arrangement is shown in Fig. 1. The x-ray beam coming from the source impinged on the phase modulator mounted on a linear translation stage at a distance of approximately 56 cm from the source. The phase modulator was a sheet of P800 grade sandpaper with a nominal average grain size of 21.8 ± 1.0 μm [29].

The sample was placed 14 cm downstream of the phase modulator (source-sample distance ∼70 cm). The detector system was composed of a scintillation screen, here a 600-μm-thick cerium-doped gadolinium aluminum gallium garnet (GAGG:Ce) crystal, for conversion of x-rays to visible light, coupled to an optical microscope and a scientific CMOS (sCMOS) camera (pco.edge 4.2; chip size 2048 × 2048 pixels; pixel size 6.5 μm). The microscope system was produced by Optique Peter (Lentilly, France) and contained a 2× magnifying objective, leading to an effective detector pixel size of 3.25 μm.

The source–scintillator distance was approximately 81 cm, resulting in a sample–scintillator distance of approximately 11 cm. This configuration led to a geometric magnification of the sample of approximately 1.16 and hence an effective pixel size in the sample plane of approximately 2.8 μm. Furthermore, features in the diffuser plane were magnified by a factor of 1.45 in the detector plane and by a factor of 1.25 in the sample plane.

The sample was a true bug, a specimen of the species *Orius niger* of the family Anthocoridae, which are also known as minute pirate bugs or flower bugs. It was approximately 3.8 mm long and 1.8 mm wide. Bugs from the *Orius* genus have proven to be effective for biological pest control and are hence of interest for the agriculture sector [30,31].

Scanning was performed following the UMPA scheme [25]. Although regular unidirectional stepping is not required for UMPA, the phase modulator was stepped vertically, with a fixed step size of 75.95 μm (significantly larger than the speckle size), because of temporary experimental constraints. The data were acquired at $N = 40$ positions of the phase modulator with and without the sample in the beam. Every seven diffuser positions,

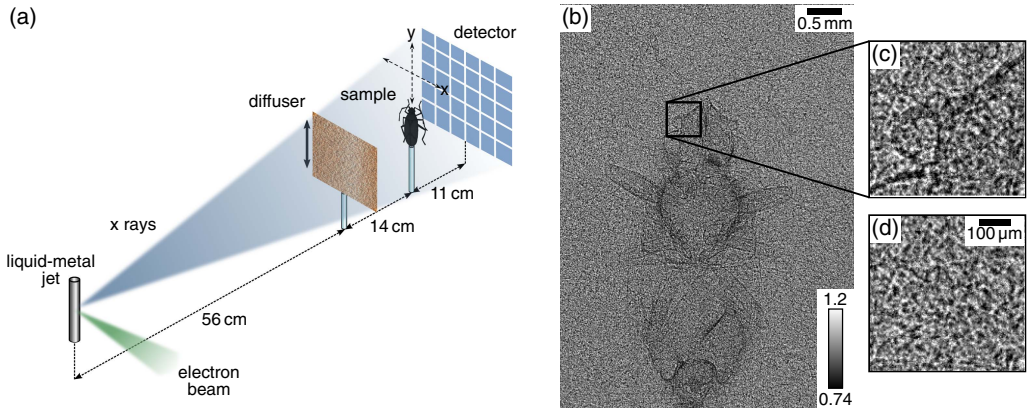

Fig. 1. (a) Experimental setup. X rays from the liquid-metal-jet source impinge first onto the diffuser mounted on a translation stage and then, further downstream, onto the sample. Images are recorded at different diffuser positions by a scintillator-coupled sCMOS detector. (b) Example of a speckle pattern recorded with the specimen in the beam; (c) ROI of (b), as indicated by the box; (d) corresponding ROI of the reference image without the sample in the beam. The speckles are modulated by the presence of the specimen, encoding transmission, differential phase, and small-angle scattering information.

the sample and phase modulator were moved out of the beam and three flat-field images were acquired. At the end of the UMPA scan, 30 dark images were collected. The exposure time for each acquired sample, reference, flat-field, and dark image was 1100 s, as a result of summing 110 frames of 10 s exposure each.

3. SPECKLE CHARACTERIZATION

The reference and sample images were dark-current and flat-field corrected. For this, the average of the dark images and of the flat-field images was determined. The average dark signal was subtracted from all frames, and subsequently the reference and sample images were divided by the dark-corrected flat-field images. Each flat-field image was used to correct the previous four and the following three reference and sample images. This ensured empty-beam correction with the flat-field image closest in time to the reference and sample images.

In a second preprocessing step, dead pixels and bright pixels in the flat-field-corrected frames, caused by direct hits to the sensor by scattered x-rays, were removed from the images using a mask. They were replaced by the median value in a 5×5 pixel window around the affected pixel.

The measurement of the speckle visibility and size is considered as a figure of merit of the capabilities of the setup [22]. The reference speckle pattern created by the illumination of the phase modulator only is shown in Fig. 2(a), and in more detail in the region of interest (ROI) of 150×150 pixels in Fig. 2(b). In a first qualitative visual assessment, the speckle pattern appears to be uniform, and the speckles are of high visibility.

The speckle visibility v was analyzed quantitatively in a 150×150 pixel region around each pixel as

$$v = \frac{\sigma_I}{\bar{I}}, \tag{1}$$

where σ_I and $\bar{I}$ are the standard deviation and the mean intensity value, respectively, of the speckle pattern in the ROI, as used, for example, in Refs. [20,32–34]. The visibility map obtained this way is displayed in Fig. 2(c). The average speckle visibility over the field of view is $v = (11.0 \pm 0.5)\%$, which is comparable, but slightly lower, to the speckle visibility in the range 15%–20% achieved with a similar setup [20] with better transverse coherence conditions but lower spatial resolution. A gradient in the visibility map is detected, which is probably caused by a slight tilt of the scintillator. The size of the speckles was determined via two-dimensional (2D) autocorrelation of the reference speckle pattern, and the full width at half-maximum (FWHM) of the autocorrelation peak was taken as a measure of the speckle size [20]. Horizontal and vertical line profiles through the center of the 2D autocorrelation of the speckle pattern were fitted by Gaussians to determine the FWHM. The resulting speckle size was approximately 3.20 pixels in the horizontal and 3.24 pixels in the vertical direction, corresponding to 10.4 μm and 10.5 μm, respectively, in the detector plane.

4. PHASE-CONTRAST AND DARK-FIELD IMAGES

Before extraction of the differential phase, dark-field, and transmission signals, slight drifts of the phase modulator between sample and reference frames were eliminated by aligning the reference to the corresponding sample image at each diffuser position by performing cross correlation in a background region consisting only of the unmodified speckle pattern (here a region in air).

The reconstruction of the multimodal image signals was then carried out using a C implementation of the UMPA analysis code [35] with a window size of 5×5 pixels as a compromise between spatial resolution and sensitivity [25]. From the UMPA model, the differential phase signals in x and y, which are directly proportional to the refraction angle, are obtained from the displacement of the speckles in those directions. The speckle displacement s retrieved by UMPA is converted into the refraction angle α for each direction separately via geometric considerations:

$$\alpha = \frac{s}{d}, \tag{2}$$

where d is the sample–scintillator distance. The dark-field signal is computed from the local decrease in speckle visibility, while the transmission image is given by the decrease in average intensity in the analysis window. The transmission image obtained

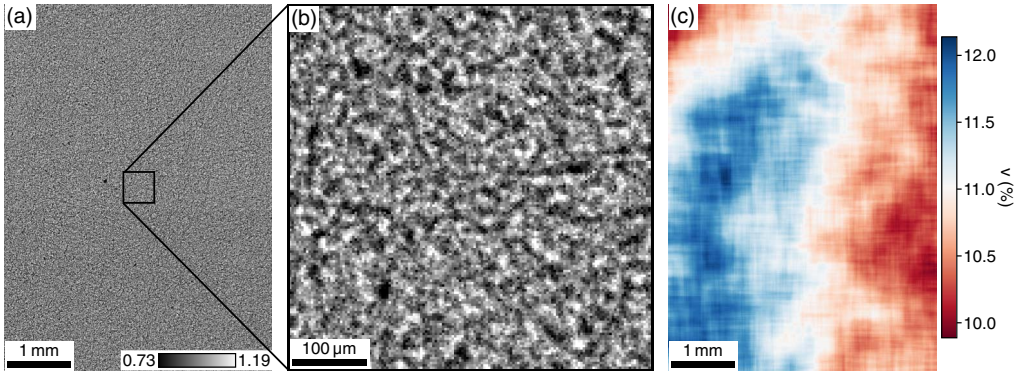

Fig. 2. Characteristics of the speckle interference pattern created by illumination of a piece of P800 sandpaper at a liquid-metal-jet x-ray source. (a) Reference speckle pattern, (b) ROI in the center of the field of view (150×150 pixels). The speckle size determined from a 2D autocorrelation analysis is 10.4 μm in the horizontal and 10.5 μm in the vertical direction. (c) Visibility map of the speckle pattern in (a). The average visibility over the field of view is $(11.0 \pm 0.5)\%$.

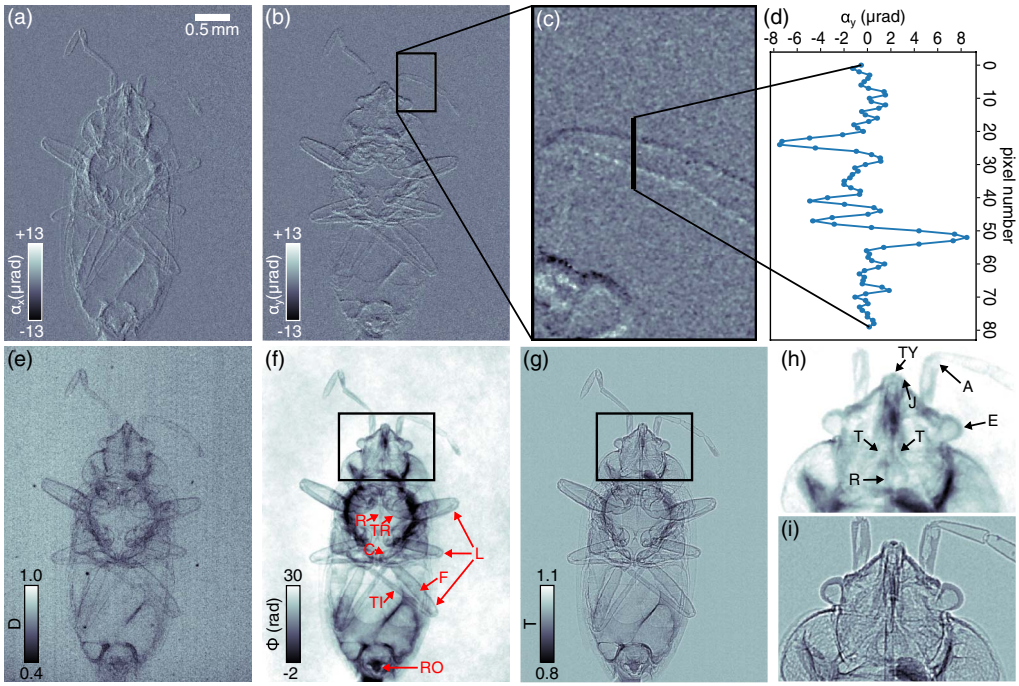

Fig. 3. Multimodal radiographs of the bug obtained with the UMPA for speckle-based imaging at a laboratory source. (a) Horizontal and (b) vertical refraction angle images; (c) ROI highlighting the location of the profile used to determine the spatial resolution and (d) line profile across the bug's antenna as indicated in (c), giving an estimation of the spatial resolution of approximately 5 pixels; (e) dark-field, (f) integrated phase with labeled features, and (g) transmission image of the bug; (h), (i) ROIs of the phase and transmission signals, respectively, as indicated by the boxes in panels (f) and (g). Details of the bug's head can be observed. Labels are explained in the main text.

this way is similar to the image that would have been recorded without the diffuser in the beam and contains both the absorption and edge-enhancement signals. The latter is proportional to the second derivative of the phase and originates from free-space propagation of the x-rays from the sample to the detector plane.

Phase integration from the differential phase projections was carried out using a Fourier integration routine [36] including the two differential phase signals in the horizontal and vertical directions. A fourth-order polynomial was fitted to the air background region of the reconstructed integrated phase signal and subtracted to eliminate low-frequency artifacts that can arise during the integration step, in particular in the presence of noise.

The resulting projections of the bug sample are shown in Fig. 3. As expected, while mostly vertical features are visible in the horizontal refraction angle signal in Fig. 3(a), the vertical refraction angle in Fig. 3(b) shows horizontal features. In Fig. 3(e), the dark-field image highlights the edges of the specimen. A non-negligible dark-field signal can also be observed inside the sample, particularly in thicker areas of the specimen, which can be attributed mainly to beam-hardening effects [32].

The phase signal, integrated from the differential phase in Figs. 3(a) and 3(b), and the transmission image are shown in Figs. 3(f) and 3(g), respectively. Both modalities clearly visualize small features of the specimen's body, as labeled for the right side of the bug in Fig. 3(f). Furthermore, details of the head can be observed, as shown in more detail in the ROIs in Figs. 3(h) and 3(i): the tylus (TY), the forward-projecting part at the front of the head, and the juga (J), the outer lobes at the front of the head. The mouth part contains the rostrum (R), which extends downward and is a long beak with a sharp tip that the bug uses for sucking plants or insect prey after injecting them with digestive enzymes. The antennae (A) consist of four segments, as is typical for bugs of the Anthocoridae family. Variations in density can be observed for the different segments and are most likely due to drying of the specimen, which left the right antenna almost hollow. The compound eyes (E) are denser on the outside than the inside. Interestingly, even two of the head tracheae (T) can be observed. These tubes that run through the entire body of the bug deliver oxygen and are an essential part of the respiratory system. Details of the structure of the legs (L) with their various segments can be seen in Figs. 3(f) and 3(g). The leg is attached to the main body at the coxa (C), which is followed by the trochanter (TR), the thick femur (F), and the tibia (TI). The last segment of the leg, here partly covered by overlaying structures, is the tarsus. At the bottom of the bug's body, the reproductive organ (RO) is visible.

The background around the bug in the differential phase images was used to determine the angular sensitivity, i.e., the resolution of the refraction angle measurement, as the ratio of standard deviation and mean signal in 29 ROIs of 150 × 150 pixels each. The average sensitivity is 1.33 ± 0.24 μrad in x and 1.30 ± 0.17 μrad in y. The sensitivity is slightly better in the vertical than in the horizontal direction due to the mounting of the diffuser on a vertically oriented post, which makes the diffuser more stable in the vertical direction.

An upper limit to the spatial resolution was estimated from the differential phase image analogously to the procedure in

Ref. [24] by taking the FWHM of the line profile across one of the antennae of the bug; see Figs. 3(c) and 3(d). The width of approximately 5 pixels of the edges of the antenna corresponds to 14 μm in the sample plane. The spatial resolution of the final images is limited by the extent of the Hamming function used in the analysis window for the UMPA reconstruction, the point spread function of the detector system, and the blurring by the projected source size. For the phase image, it is also affected by the low-pass nature of the phase-integration routine [36].

5. DISCUSSION AND CONCLUSIONS

Previous implementations of SBI at laboratory sources have been reported using the single-shot speckle-tracking mode [19,20] or the speckle-scanning mode [24]. The experiments performed with speckle tracking are in general faster, but they provide data with a spatial resolution limited by the relatively large window size, which needs to exceed the extent of a speckle for single-shot imaging.

In the work by Zhou *et al.* [24] with a setup similar to the one used in the presented experiment, the authors obtained multimodal projection images of a spider leg with the speckle-scanning technique and a total of 900 diffuser steps. The scanning motor had to be moved with submicrometer precision. Excellent results have been obtained in Ref. [24], with a spatial resolution down to 7 μm. However, the impracticality of this implementation due to the large number of frames and the instrumentation required for the measurement has prevented its adoption by the user community.

A hybrid between the speckle-scanning and speckle-tracking methods was used for medium-resolution laboratory measurements by Wang *et al.* [37]. They performed one-directional speckle-scanning with 60 steps, resulting in direction-dependent sensitivity and spatial resolution that are typically superior to the speckle-tracking case but cannot reach the level of 2D speckle-scanning data. The measurements reported in Ref. [37] are considerably faster (exposure time per frame is under 1 s) than those performed in our work or in Ref. [24], but Wang *et al.* used a flat-panel detector with a much larger pixel size of 200 μm (34.9 μm effective pixel size in the sample plane) in combination with a source power of 22.5 W, more than double the power used for our measurements-at the cost of a larger x-ray spot size of 20 μm × 20 μm.

Even though, as in Ref. [37], we also performed one-directional scanning because of experimental constraints, this is not a requirement for UMPA. Unlike the conventional speckle-scanning method, UMPA does not rely on accurate scanning with sub-speckle step sizes of the phase modulator, and the step positions do not need to follow a regular raster. Shifts of the speckle pattern between the reference and corresponding sample images can be corrected for by realigning the images in a background region without the sample, which relaxes the demands on the motor precision and makes UMPA robust to setup instabilities. Moreover, compared to other scanning-based methods, UMPA in general allows retrieval of the multimodal images from a smaller number of frames. The sensitivity and spatial resolution provided by UMPA are independent of the scanning direction and are tuned by choosing the size of the analysis window. A larger window size results in a gain in refraction angle sensitivity at the expense of spatial resolution, as explained in detail in Ref. [25].

In general, the sensitivity and spatial resolution of laboratory implementations of x-ray phase-contrast imaging, including UMPA, are lower than for synchrotron data due to the significantly lower brilliance. The sensitivity of our results is estimated to be decreased by approximately four times compared to data acquired under similar conditions at the synchrotron. We expect a significant improvement in image quality after the optimization of the setup that is currently underway, with the goal to reduce scan time and increase the speckle visibility and angular sensitivity. In order to achieve this, a detector system with a more efficient scintillation screen and larger pixels will be installed. Additionally, the shape of the electron spot will be optimized and the hutch geometry modified to allow for longer propagation distances.

We believe that this proof-of-principle study demonstrates that the UMPA of speckle data is the ideal candidate for the implementation of SBI at laboratory sources for a broad range of imaging applications and optics characterization, that is accessible to a wide user community. While we have here illustrated the first (to our knowledge) lab-based realization of the technique for 2D projection imaging, the extension to tomography studies to explore the 3D inner structure of specimens will be possible once the setup has been optimized to allow for shorter exposure times.

Funding. Royal Society (RGF/EA/181028, URF/R1/180760); European Research Council (279753); H2020 European Research Council (714697).

Acknowledgment. I. Z. and M.-C. Z. are funded by a Royal Society University Research Fellowship and Enhancement Award. P. T. acknowledges funding by the European Research Council (ERC) under the project "OptImaX" (grant agreement no. 279753). N. W. P. acknowledges funding from the ERC under the European Union's Horizon 2020 research and innovation program under the project "AtoFun" (grant agreement no. 714697).

Disclosures. The authors declare no conflicts of interest.

REFERENCES

1. B. Metscher, "MicroCT for developmental biology: a versatile tool for high-contrast 3D imaging at histological resolutions," Dev. Dyn. **238**, 632–640 (2009).
2. M. Wong, A. Dorr, J. Walls, J. Lerch, and M. Henkelman, "A novel 3D mouse embryo atlas based on micro-CT," Development **139**, 3248–3256 (2012).
3. J. Martins de Souza e Silva, I. Zanette, P. B. Noël, M. B. Cardoso, M. A. Kimm, and F. Pfeiffer, "Three-dimensional non-destructive soft-tissue visualization with X-ray staining micro-tomography," Sci. Rep. **5**, 14088 (2015).
4. S. W. Wilkins, T. E. Gureyev, D. Gao, A. Pogany, and A. W. Stevenson, "Phase-contrast imaging using polychromatic hard x-rays," Nature **384**, 335–337 (1996).
5. A. Snigirev, I. Snigireva, V. Kohn, S. Kuznetsov, and I. Schelokov, "On the possibilities of x-ray phase contrast microimaging by coherent high-energy synchrotron radiation," Rev. Sci. Instrum. **66**, 5486–5492 (1995).

6. U. Bonse and M. Hart, "An x-ray interferometer," Appl. Phys. Lett. **6**, 155–156 (1965).
7. T. J. Davis, D. Gao, T. E. Gureyev, A. W. Stevenson, and S. W. Wilkins, "Phase-contrast imaging of weakly absorbing materials using hard x-rays," Nature **373**, 595–598 (1995).
8. C. David, B. Nöhammer, H. H. Solak, and E. Ziegler, "Differential x-ray phase contrast imaging using a shearing interferometer," Appl. Phys. Lett. **81**, 3287–3289 (2002).
9. A. Olivo and R. Speller, "A coded-aperture technique allowing x-ray phase contrast imaging with conventional sources," Appl. Phys. Lett. **91**, 074106 (2007).
10. S. Bérujon, H. Wang, and K. Sawhney, "X-ray multimodal imaging using a random-phase object," Phys. Rev. A **86**, 063813 (2012).
11. K. S. Morgan, D. M. Paganin, and K. K. W. Siu, "X-ray phase imaging with a paper analyzer," Appl. Phys. Lett. **100**, 124102 (2012).
12. M.-C. Zdora, J. Vila-Comamala, G. Schulz, A. Khimchenko, A. Hipp, A. C. Cook, D. Dilg, C. David, C. Grünzweig, C. Rau, P. Thibault, and I. Zanette, "X-ray phase microtomography with a single grating for high-throughput investigations of biological tissue," Biomed. Opt. Express **8**, 1257–1270 (2017).
13. H. Dejea, P. Garcia-Canadilla, A. C. Cook, E. Guasch, M. Zamora, F. Crispi, M. Stampanoni, B. Bijnens, and A. Bonnin, "Comprehensive analysis of animal models of cardiovascular disease using multiscale x-ray phase contrast tomography," Sci. Rep. **9**, 6996 (2019).
14. H. Wang, R. C. Atwood, M. J. Pankhurst, Y. Kashyap, B. Cai, T. Zhou, P. D. Lee, M. Drakopoulos, and K. Sawhney, "High-energy, high-resolution, fly-scan x-ray phase tomography," Sci. Rep. **9**, 8913 (2019).
15. H. Dutel, M. Galland, P. Tafforeau, J. A. Long, M. J. Fagan, P. Janvier, A. Herrel, M. D. Santin, G. Clément, and M. Herbin, "Neurocranial development of the coelacanth and the evolution of the sarcopterygian head," Nature **569**, 556–559 (2019).
16. C. B. Cannata, R. De Rosa, P. Donato, S. Donato, G. Lanzafame, L. Mancini, and B. F. Houghton, "First 3D imaging characterization of Pele's hair from Kilauea volcano (Hawaii)," Sci. Rep. **9**, 1711 (2019).
17. C. Liu, A. Das, W. Wang, S. Küchemann, P. Kenesei, and R. Maass, "Shear-band cavities and strain hardening in a metallic glass revealed with phase-contrast x-ray tomography," Scripta Mater. **170**, 29–33 (2019).
18. F. Pfeiffer, T. Weitkamp, O. Bunk, and C. David, "Phase retrieval and differential phase-contrast imaging with low-brilliance x-ray sources," Nat. Phys. **2**, 258–261 (2006).
19. I. Zanette, T. Zhou, A. Burvall, U. Lundström, D. H. Larsson, M.-C. Zdora, P. Thibault, F. Pfeiffer, and H. M. Hertz, "Speckle-based x-ray phase-contrast and dark-field imaging with a laboratory source," Phys. Rev. Lett. **112**, 253903 (2014).
20. I. Zanette, M.-C. Zdora, T. Zhou, A. Burvall, D. H. Larsson, P. Thibault, H. M. Hertz, and F. Pfeiffer, "X-ray microtomography using correlation of near-field speckles for material characterization," Proc. Natl. Acad. Sci. USA **112**, 12569–12573 (2015).
21. R. Cerbino, L. Peverini, M. A. C. Potenza, A. Robert, P. Bösecke, and M. Giglio, "X-ray-scattering information obtained from near-field speckle," Nat. Phys. **4**, 238–243 (2008).
22. M.-C. Zdora, "State of the art of x-ray speckle-based phase-contrast and dark-field imaging," J. Imaging **4**, 60 (2018).
23. S. Berujon, E. Ziegler, R. Cerbino, and L. Peverini, "Two-dimensional x-ray beam phase sensing," Phys. Rev. Lett. **108**, 158102 (2012).
24. T. Zhou, I. Zanette, M.-C. Zdora, U. Lundström, D. H. Larsson, H. M. Hertz, F. Pfeiffer, and A. Burvall, "Speckle-based x-ray phase-contrast imaging with a laboratory source and the scanning technique," Opt. Lett. **40**, 2822–2825 (2015).
25. M.-C. Zdora, P. Thibault, T. Zhou, F. J. Koch, J. Romell, S. Sala, A. Last, C. Rau, and I. Zanette, "X-ray phase-contrast imaging and metrology through unified modulated pattern analysis," Phys. Rev. Lett. **118**, 203903 (2017).
26. M.-C. Zdora, I. Zanette, T. Zhou, F. J. Koch, J. Romell, S. Sala, A. Last, Y. Ohishi, N. Hirao, C. Rau, and P. Thibault, "At-wavelength optics characterisation via x-ray speckle- and grating-based unified modulated pattern analysis," Opt. Express **26**, 4989–5004 (2018).
27. M.-C. Zdora, P. Thibault, W. Kuo, V. Fernandez, H. Deyhle, J. Vila-Comamala, M. P. Olbinado, A. Rack, P. M. Lackie, O. L. Katsamenis, M. J. Lawson, V. Kurtcuoglu, C. Rau, F. Pfeiffer, and I. Zanette, "Three-dimensional virtual histology with x-ray near-field speckles," (to be published).
28. Excillum, "Metal Jet D2 Data Sheet," 2019, https://www.excillum.com/products/metaljet-sources/metaljet-d2-160-kv/.
29. Federation of European Producers of Abrasives, "FEPA P-grit sizes coated abrasives," 2019, https://www.fepa-abrasives.com/abrasive-products/grains.
30. M. Van de Veire and D. Degheele, "Biological control of the western flower thrips, *Frankliniella occidentalis* (Pergande) (Thysanoptera: Thripidae), in glasshouse sweet peppers with *Orius* spp. (Hemiptera: Anthocoridae). A comparative study between *O. niger* (Wolff) and *O. insidiosus* (Say)," Biocontrol Sci. Technol. **2**, 281–283 (1992).
31. P. N. Deligeorgidis, "Predatory effect of *Orius niger* (Wolff) (Hem., Anthocoridae) on *Frankliniella occidentalis* (Pergande) and *Thrips tabaci* Lindeman (Thysan., Thripidae)," J. Appl. Entomol. **126**, 82–85 (2002).
32. M.-C. Zdora, P. Thibault, F. Pfeiffer, and I. Zanette, "Simulations of x-ray speckle-based dark-field and phase-contrast imaging with a polychromatic beam," J. Appl. Phys. **118**, 113105 (2015).
33. S. Bérujon and E. Ziegler, "X-ray multimodal tomography using speckle-vector tracking," Phys. Rev. Appl. **5**, 044014 (2016).
34. H. Wang, Y. Kashyap, B. Cai, and K. Sawhney, "High energy x-ray phase and dark-field imaging using a random absorption mask," Sci. Rep. **6**, 30581 (2016).
35. Code available at: https://github.com/pierrethibault/UMPA.
36. C. Kottler, C. David, F. Pfeiffer, and O. Bunk, "A two-directional approach for grating-based differential phase contrast-imaging using hard x-rays," Opt. Express **15**, 1175–1181 (2007).
37. H. Wang, Y. Kashyap, and K. Sawhney, "From synchrotron radiation to lab source: advanced speckle-based x-ray imaging using abrasive paper," Sci. Rep. **6**, 20476 (2016).